ACS Catalysis

Research Article

Cite This: ACS Catal. 2019, 9, 5074−5083

pubs.acs.org/acscatalysis

A-site Excessive $(La_{0.8}Sr_{0.2})_{1+x}MnO_3$ Perovskite Oxides for Bifunctional Oxygen Catalyst in Alkaline Media

Weichuan Xu,[†] Nicholas Apodaca,[‡] Haizhen Wang,[†] Litao Yan,[†] Gen Chen,[†] Meng Zhou,*[,†] Dong Ding,*[,§] Pabitra Choudhury,*[,‡] and Hongmei Luo*[,†]

[†]Chemical and Materials Engineering Department, New Mexico State University, Las Cruces, New Mexico 88003, United States

[‡]Chemical and Materials Engineering Departments, New Mexico Tech, Socorro, New Mexico 87801, United States

[§]Energy & Environment Science and Technology, Idaho National Laboratory, Idaho Falls, Idaho 83415, United States

Supporting Information

ABSTRACT: Nominal A-site excessive $(La_{0.8}Sr_{0.2})_{1+x}MnO_3$ (x = 0, 0.05, and 0.1) (denoted as LSM, LS1.05M, and LS1.1M) perovskite oxides have been synthesized by the polymer-assisted chemical solution (PACS) method for bifunctional oxygen electrocatalysis, including both oxygen reduction reaction (ORR) and oxygen evolution reaction (OER) applications in alkaline media. LS1.05M exhibits 21% higher diffusion-controlled ORR current density, 87% higher OER current density at 0.8 V (vs Ag/AgCl 3.5 M), and ultralow electrochemical impedance compared to pristine LSM. LS1.1M has mixed performance relative to LSM due to structure instability. First-principles study by density functional theory (DFT) suggests that the free energy decrease from O* to *OOH is the rate-limiting step in OER. Transition metal d-band center and oxygen p-band center approaching the Fermi level are responsible for the enhanced electrochemical activity.

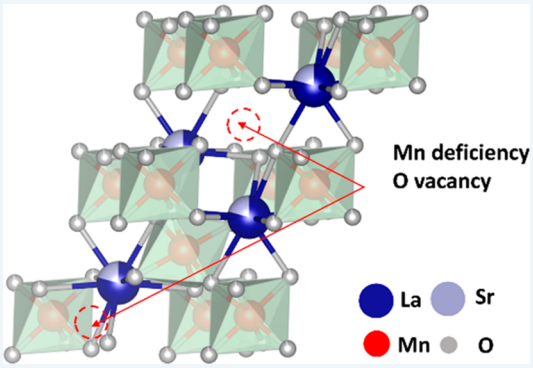

KEYWORDS: *A-site excess, first-principles, perovskite catalyst, bifunctional, polymer-assisted*

1. INTRODUCTION

The increasing demands on clean, renewable energy with abundant resources as an alternative to fossil fuel are pushing the limit of novel catalysts in energy conversion devices. The cathode materials for a fuel cell and anode materials for a water electrolyzer still face challenges of catalyzing the oxygen reduction reaction (ORR) and oxygen evolution reaction (OER), respectively. Currently, the leading catalyst in alkaline electrolyte for ORR is platinum (Pt/C), while that in acidic media for OER is iridium oxide (IrO_2)/ruthenium oxide (RuO_2). For development of unitized regenerative fuel cells, solid state fuel cells, and rechargeable metal−air batteries, oxygen bifunctionality is required for electrocatalysts used in these electrochemical systems. However, there are some challenges of Pt/C displaying unsatisfactory OER performance due to metal oxide formation on the electrode surface,[1,2] and IrO_2 presents no intrinsic properties of ORR kinetics.[3] Besides, the prohibitive cost and scarcity of noble metals exclude them from cost-effective bifunctional catalysts. Therefore, the development of inexpensive and efficient bifunctional catalysts is of imminent significance.

Transition metal (TM) oxide with perovskite ABO_3 crystal structure has been identified as a candidate for the bifunctional catalyst. It has the tolerance of cation and oxygen defect without a significant change of lattice structure. A-site rare-earth or alkaline cations have coordination number of 12 with oxygen, while B-site transition metal elements form 6-fold octahedron with oxygen. Due to the tunable composition and thus the crystal structure of perovskites, leading to different properties, several strategies have been examined to modify the perovskites. The common methods include A-site doping, B-site doping,[4,5] nonstoichiometric A-site deficiency/excess,[6−10] morphology tuning, and synergistic combination with other materials.[11−14]

Unfortunately, most perovskite catalysts have electronic structure favored for only ORR or OER. Catalyst bifunctionality is realized by carefully tailoring the electronic environment of metal cations and oxygen anions. Catalytic performance of perovskite is explained by metal 3d orbital and oxygen 2p orbital hybridizing configuration in terms of B−O bond strength, oxidation valence of B-site cation, content of lattice oxygen, and oxygen species absorbed in lattice defects. The most widely used method for regulating perovskite catalysts performance is cation doping. A-site doping influences the amount of oxygen species, while the B-site doping changes the type of oxygen species and B−O bonds.[15,16] Wang et al. reported enhanced bifunctional catalyst and lithium−air battery performance for Sr and Ni-doped $La_{0.8}Sr_{0.2}Mn_{1-x}Ni_xO_3$

Received: February 22, 2019
Revised: April 25, 2019
Published: April 26, 2019

DOI: 10.1021/acscatal.9b00800
ACS Catal. 2019, 9, 5074−5083

due to the increased content of alpha-oxygen and Mn^{4+}cation.[17] Merino et al. suggested the propane combustion by Ca-doped $La_{1-x}Ca_xCoO_3$ is related to the absorbed electrophilic oxygen species on surface oxygen vacancy.[16] The vast combination of cation doping greatly enriches the study of perovskite catalysts.

A-site nonstoichiometry is another simple way for tuning the physical and chemical properties of perovskite catalyst, often involving A-site deficiency or A-site excess design. The deficient A-site cation in perovskite lattice is compensated by either promoted oxidation valence of B-site cation or introduction of oxygen vacancy to balance out extra charges. In our previous work, $(La_{0.8}Sr_{0.2})_{0.95}Mn_{0.95}Ir_{0.05}O_3$ with a combination of A-site deficiency and Ir-doping demonstrated a weakened Mn−O transition metal−oxygen bond and 200 mV reduced OER onset potential.[18]

A-site excess, however, is rarely reported in the perovskite research field. Reports of A-site excess perovskites focus on oxygen incorporation/evolution in solid oxide fuel cell (SOFC) electrodes,[6,19,20] an oxygen permeable membrane,[8] application in fuel catalytic oxidation,[21] and dielectric properties in a conduction mechanism study.[22−24] A small amount of A-site cation oxide phase segregation could be observed to compensate B-site cation loss during preparation.[22] Zhang's group reported 5% excess $(Pr_{0.4})_{1.05}Sr_{0.6}Co_{0.2}Fe_{0.7}Nb_{0.1}O_{3-\delta}$ has the lowest polarization resistance in both O_2 and wet H_2, and the fabricated symmetric SOFC with this material reached maximum power density.[6] Chen and his colleagues found that nonstoichiometric $La_{1.05}MnO_3$ exhibits better activity toward NO oxidation because of active oxygen species near Mn^{4+} cations.[21] Improved sintering, decreased tangent loss, and enhanced piezoelectric, electromechanical properties were observed for A-site excess $Bi_{0.5}Na_{0.5}TiO_3$.[22] In particular, reduced bulk resistance due to high oxide-ion conductivity makes A-site excess $Bi_{0.5}Na_{0.5}TiO_3$ good candidates as electrode materials for SOFC, solar fuel cells, electrolyzers, and other energy devices.[22] However, no research was reported on room temperature ORR/OER by A-site excessive perovskite catalysts. Also, despite the fact of first-principles studies on defect perovskite, there is nearly no simulation result on A-site excessive perovskite related materials.

Mn-based perovskites have shown good performance toward ORR while relatively poor activity to OER.[25,26] As illustrated in our previous research, $La_{0.8}Sr_{0.2}MnO_3$ perovskite as a robust ORR catalyst displayed the potential of catalyzing OER with a modification.[18,27] Adapted from polymer-assisted deposition (PAD) for crack-free thin film synthesis,[28] our polymer-assisted chemical solution (PACS) method for powder perovskite catalyst preparation shows the ability to afford nanoscale grain size and enhanced electrochemical and catalytic performance compared to $La_{0.8}Sr_{0.2}MnO_3$ by the conventional sol−gel method.[27] Conversely, the conventional synthesis process of perovskite is dominated by a solid state reaction or citric acid-aided sol−gel method, followed by calcination at high temperature (~1000 °C), resulting in particle aggregation to several micrometers. Besides, no conductive carbon is needed when preparing catalyst ink using the perovskites obtained from PACS. The ORR and OER performances have been widely reported with perovskite of doping and A-site deficiency configurations. To the best of our knowledge, no paper on A-site excess perovskite for bifunctional oxygen electrocatalysis in alkaline media is available. We herein introduce the PACS synthesis of A-site excessive $(La_{0.8}Sr_{0.2})_{1+x}MnO_3$ (x = 0, 0.05, and 0.1) for room temperature ORR and OER. Besides, OERs on the perovskite surface, along with the metal 3d band center and oxygen 2p center positions relative to the Fermi level, are calculated to find the root of improved performance.

2. METHODOLOGY

2.1. Synthesis. $(La_{0.8}Sr_{0.2})_{1+x}MnO_{3-\delta}$ (x = 0, 0.05, and 0.1, denoted as LSM, LS1.05M, and LS1.1M, respectively) were synthesized with an optimized polymer-assisted chemical solution method. Typically, for 1 mmol of LSM, 2 g of poly(ethylenimine) (PEI solution ~50% in H_2O, Sigma-Aldrich), 1 g of ethylenediaminetetraacetic acid (EDTA, Sigma-Aldrich), and 10 mL of DI water were mixed and stirred in a beaker until a clear solution was formed. Then, 0.346 g of lanthanum(III) nitrate hexahydrate (99+%, Sigma-Aldrich), 0.042 g of strontium nitrate (99+%, A.C.S. reagent, Sigma-Aldrich), and 0.245 g of manganese(II) acetate tetrahydrate (Sigma-Aldrich) were added to the solution and stirred for 1 h. The solution was further heated in a furnace in air at 150 °C for 2 h to evaporate excessive water. Finally, the sample was heated at 650 °C for 3 h for perovskite structure formation. For the preparation of A-site excess samples, the amounts of lanthanum(III) nitrate hexahydrate and strontium nitrate were increased to 0.363 and 0.044 g for LS1.05M and 0.381 and 0.046 g for LS1.1M, respectively.

2.2. Physical Characterization. Phase identification and crystallography were conducted using X-ray diffraction (XRD, Empyrean series 2, PANalytical) with a Cu Kα radiation of 1.54059 Å. XRD Rietveld refinement was analyzed by Maud software (Material Analysis Using Diffraction). Inductively coupled plasma (ICP) was carried out by the Octopole Reaction System (ORS) Agilent 7500ce with a CETAC XS-520 autosampler for composition analysis. The microstructure and morphology were examined using transmission electron microscopy (TEM, H7650, Hitachi) operated at 80 kV. For detailed information on sample structure and lattice parameters, high-resolution transmission electron microscopy (HRTEM) and selected area electron diffraction (SAED, JEM- 2100, JEOL) were used, operated at 200 kV. Elemental mapping along with catalyst bulk composition determination were carried out on a scanning electron microscope (SEM) equipped with energy-dispersive X-ray spectroscopy (EDX, S-3400 Type II, Hitachi). X-ray fluorescence (XRF) was carried out on a FISCHER X-ray XDV-SDD energy-dispersive fluorescence measuring instrument. The surface areas of the samples were examined by the Brunauer−Emmett−Teller (BET) with a Micromeritics ASAP 2050 instrument using the standard N_2 adsorption and desorption isotherm measurement at 77 K. Thermogravimetric analysis (TGA) was carried out by PerkinElmer Pyris 1 from room temperature to 1000 °C at the heating rate of 10 °C/min in oxygen. The surface chemistry and lattice defect were studied on X-ray photoelectron spectroscopy (XPS, Scientific K-Alpha, Thermo) with a monochromatic Al Kα source.

2.3. Electrochemical Characterization. All electrochemical tests were conducted with a CHI 760C workstation and standard three-electrode setup (PINE instrument) at room temperature, including working electrode, Ag/AgCl (3.5 M) reference electrode, and Pt coil counter electrode. The catalyst powder was dissolved in 0.05 wt % Nafion solution to a concentration of 5 mg/mL. The catalyst solution was sonicated for 20 min until a homogeneous ink was formed. Then, 10 μL

DOI: 10.1021/acscatal.9b00800
ACS Catal. 2019, 9, 5074−5083

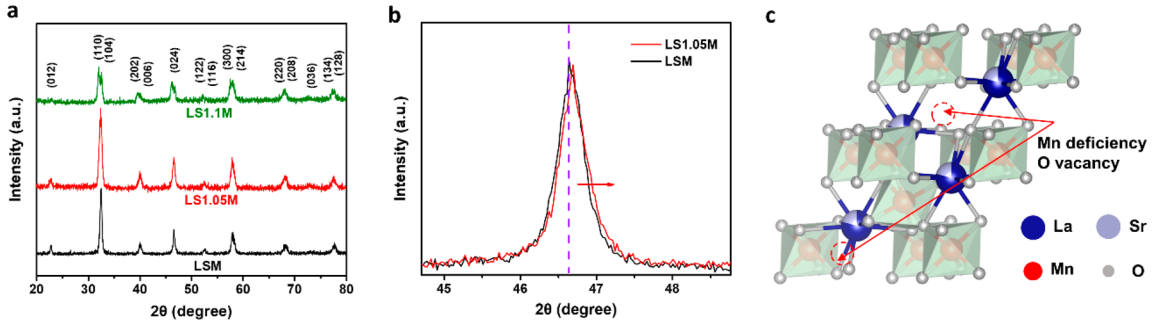

Figure 1. (a) XRD of LSM, LS1.05M, and LS1.1M and (b) regional XRD of LSM and LS1.05M; (c) perovskite with Mn and O deficiency.

of ink was cast on a glassy carbon (GC) electrode with an area of 0.195 cm^2 and dried at 50 °C for 30 min. The GC electrode was polished with 5, 0.3, and 0.05 μm alumina solution in sequence and cleaned with DI water before each use. The linear sweep voltammetry (LSV) for the oxygen reduction reaction (ORR), oxygen evolution reaction (OER), and electrochemical impedance spectroscopy (EIS) together with chronoamperometry (CA) was measured in 0.1 M KOH solution. All measurement data were *iR* corrected (i.e., $E = E_0 - iR$, where E_0 is recorded potential, i is measured current density, and R is electrical resistance of the electrolyte ca. 45 Ω) except for EIS and CA.

For electron transfer number and kinetic current density analysis of ORR, the Koutecky–Levich (K-L) plot was implemented:

$$\frac{1}{J} = \frac{1}{J_K} + \frac{1}{J_D} = \frac{1}{J_K} + M\frac{1}{n}\frac{1}{w^{1/2}} \quad (1)$$

where $M = 1/[0.62FAC_{O_2}D_{O_2}^{2/3}\nu^{-1/6}]$. F is Faradaic constant (C/mol); A is electrode area (cm^2). C_{O_2} is the O_2 concentration in alkaline solution (mol/cm^3), and D_{O_2} is the O_2 diffusion coefficient in 0.1 M KOH (cm^2/s). ν is viscosity of the solution (cm^2/s); n is electron transfer number, and w is angular frequency of the electrode (rad/s). Measured current density J (A) consists of kinetic current density J_K and diffusion controlled current density J_D.

2.4. Computational Methods. Spin polarized density functional theory (DFT) calculations were carried out on an LSM(001) slab using the Perdew–Burke–Ernzerhof (PBE)[29] functional and projector augmented wave (PAW) method,[30] as implemented in the Vienna Ab initio Simulation Package (VASP).[31−33] A plane wave basis set with 550 eV energy cutoff including the van der Waals interactions proposed by Grimme[34] was used to calculate the total energy calculations for all the systems. The electronic energy of 10^{-6} eV for the electronic relaxations and the residual forces of 0.02 eV/Å on ions for the ionic relaxations were used. We also used the Gaussian smearing with a width of 0.02 eV around the Fermi level to expedite the convergence. Initially, a six-layer LSM(001) slab structure was created from lanthanum manganite, a general form of ABO_3 type perovskite-based crystal structure, with the general formula $La_{1-x}Sr_xMnO_3$, where x describes the doping level. In the crystal, the A-sites are occupied by both La and Sr atoms and the B-sites are occupied by the smaller Mn atoms. This means that some La atoms are doped with Sr atoms randomly in a supercell with a stoichiometric ratio of 3:1 to limit the computational cost. Hence, the value of x is 0.25 for all the systems. The dimensions of the LSM supercell ($La_9Sr_3Mn_{12}O_{36}$) were 11.0066 × 11.0066 × 33.5585 Å^3. We then created the A-site excess LSM by removing one Mn atom from another supercell ($La_9Sr_3Mn_{11}O_{36}$), which has the dimensions of 11.1380 × 11.1380 × 33.5585 Å^3, to mimic the experimentally synthesized perovskite materials. Both $La_{0.75}Sr_{0.25}MnO_3$ and $La_{0.75}Sr_{0.25}Mn_{0.92}O_3$ (001) surfaces are periodic in the x and y directions, and the z dimension was chosen to be large enough so that the interactions with periodic images were negligible. A slab model was used for the optimized surfaces with a 25 Å vacuum layer separating the periodic surfaces. A gamma-point mesh was chosen to reduce the computational cost. It is to be noted that, due to errors in the prediction of M−OH, M−O, M−OOH, and M−O_2 bonding strengths during OERs in alkali medium due to the strong correlation effects in 3d transition metal oxides, the Hubbard U correction[35] was applied to Mn with a specific value of 3.96 eV.[36]

In order to evaluate the free energy profile of each elementary reaction step, we first obtained the electronic energy part of the surface bound species using the DFT+U method and, then, we incorporated the finite temperature part including the zero-point energy contribution based on the frequency calculations within the harmonic approximation, similar to our previous publication,[37] implemented in the TAMKin program.[38,39] The free energies of H_2, H_2O, and O_2 were collected from previous works.[40−42] Finally, the potential dependent free energies of the electron transfer steps were modeled using the computational hydrogen electrode (CHE) model.[42] The coupling between an electron transfer to the electrode and the formation of OH^- anion can be expressed as $(H^+ + e^-) + (OH^- - e^-) \leftrightarrow H_2O$ for the equilibrium reaction. Using the standard hydrogen electrode (SHE) as the reference electrode, the potential dependent free energy of $(OH^- - e^-)$, $G(OH^- - e^-)$, can then be determined as $G(OH^- - e^-) = G(H_2O) - G(H^+ + e^-) = G(H_2O) - 1/2G(H_2) + eV$ where V is the electrode potential. The OER mechanism on the perovskite surface in the alkali medium is known to be a 4-electron exchange mechanism:[43]

$$^*OH + OH^- \rightarrow {}^*O + H_2O + e^- \quad (2)$$

$$^*O + OH^- \rightarrow {}^*OOH + e^- \quad (3)$$

$$^*OOH + OH^- \rightarrow {}^*OO + H_2O + e^- \quad (4)$$

$$^*OO + OH^- \rightarrow {}^*OH + O_2 + e^- \quad (5)$$

where * denotes the surface bound species. Note that the bare oxide catalyst surface is not involved in this reaction mechanism in the alkali medium. In alkali medium at very high pH, the negatively charged species (OH^-) is expected to

DOI: 10.1021/acscatal.9b00800
ACS Catal. 2019, 9, 5074−5083

accumulate on the perovskite catalyst surfaces.[43,44] The corresponding free energy change for each reaction step was then calculated by taking the free energy difference between products and reactants.

3. RESULTS AND DISCUSSION

To investigate sample nanostructure and phase composition, all samples were tested with X-ray diffraction (XRD), as shown in Figure 1, and exhibited rhombohedral perovskite symmetry (space group $R\bar{3}c$), with the peaks indexed by PDF #01-0736750. Under the detection limit, no phase segregation was found. The crystallography phase difference between pristine LSM and LS1.05M is trivial, indicating similar crystallinity. Elemental analysis by ICP-ORS and SEM-EDX mapping confirm that the composition of as-prepared samples is almost consistent with the initial starting composition (Table S1 and Figures S1 and S2). Furthermore, X-ray fluorescence (XRF) was also used to determine the compositions of the as-prepared perovskites, which are listed in Table S2. Similar to SEM-EDX, XRF, a semiquantitative technique, can only be used to detect the elements on the sample surface. Thus, the compositions of perovskites measured from XRF are not as accurate those measured from ICP, which can explain why the formula of perovskites based on XRF is slightly different from that of target compounds LSM, LS1.05M, and LS1.1M; however, the result from ICP and XRF further confirms the A-site excess composition. XRD Rietveld refinement was then performed for LSM and LS1.05M with parameters listed in Table S3. The peak width of LS1.05M at 32° is broader than that of LSM, implying the smaller crystallite size of the LS1.05M. Besides, LS1.05M has a slight shift of peak position to higher θ-Bragg angles, suggesting LS1.05M lattice shrinkage compared to LSM. Excessive A-site cation and more Mn^{3+} content with larger atom size (than Mn^{4+}) for charge compensation in LS1.05M did not cause increased cell volume or peak shifting to lower degrees. To accommodate excessive A-site metal ions, B-site deficiency and oxygen vacancy are introduced in Figure 1c. Zhou et al. reported additional oxygen vacancy formation for both A-site deficient and excessive BSCF perovskite.[20,45] Though oxygen vacancy is ubiquitously discussed in A-site deficient perovskite, we infer oxygen vacancy is formed in A-site excess perovskites due to loss of manganite. The calculated lattice parameters, lattice angle, and crystallite size are listed in Table 1.

Table 1. Lattice Parameters, Lattice Angle, and Crystallite Size of LSM and LS1.05M

	a (Å)	α (degree)	crystallite size (nm)
LSM	5.51	60.00	21
LS1.05M	5.50	59.71	16
LS1.1M	5.57	59.71	11

When the A-site excessive amount reaches 10% in this study, decreased peak intensities and resolved characteristic doublets were observed at 32° for LS1.1M. Without peak indexing to any secondary phase, it is inferred that a further size mismatch of the metal cations due to nonstoichiometry occurred in the LS1.1M lattice, leading to perovskite instability with enriched electrostatic attraction between the aliovalent dopants and the oxygen vacancy on the surface.[46]

To further study the sample morphology and to directly measure the d-spacing of the samples, TEM and HRTEM with SAED were conducted for LSM and LS1.05M and shown in Figure 2. Both sample nanoparticles have sizes between 40 and 100 nm. Compared with samples with severe agglomeration prepared by the traditional sol–gel method, the products synthesized by our method show small size and high surface area (Figure S3), thus exposing more active sites for electrochemical reactions. The increased surface area of LS1.05M (26 m^2/g) and LS1.1M (26 m^2/g) as compared with LSM (19 m^2/g) indicates that more active sites can be exposed for faster reaction rate and better electrocatalytic performance. A thin layer of carbon on the surface of oxides was observed, which came from in situ polymer deposition and helped prevent the agglomeration of particles, although the carbon amount in the oxides is less than 1 wt % from TGA evaluation (Figure S4). In Figure 2b,e, lattice spacing of the (012) plane and (110) plane are 0.38 and 0.29 nm for LSM and 0.36 and 0.27 nm for LS1.05M, respectively. The decreased interplanar distances for LS1.05M agree with the XRD results, which further suggests that the excessive A-site metal ions cause atom deficiency and vacancy.

X-ray photoelectron spectroscopy (XPS) was performed to analyze the surface composition of the samples. In Figure 3a,c, the O 2p single peak for both catalysts can be deconvoluted into four subpeaks, representing lattice oxygen (O_L) at ∼529.2 eV, highly active oxygen species O_2^{2-}/O^- adsorbed to surface oxygen vacancy at ∼530.4 eV, hydroxyl group −OH at ∼531.7 eV, and physisorbed or chemisorbed water molecules (H_2O) at ∼533.2 eV.[1] Contents of each species calculated by integration of peak areas are listed in Table 2. Decreased O_L amount in LS1.05M is mainly compensated by the increase of highly active oxygen species. In Table S4, surface atomic ratio by XPS shows cation vacancy and bulk Mn deficiency to compensate electron holes.[47] The O/(La + Sr + Mn) ratio has decreased obviously as the A-site content increases, suggesting the loss of oxygen and formation of surface oxygen vacancy, consistent with the prediction from the literature.[20,48] Indeed, the loss of oxygen at high temperature (above 800 °C) for LS1.05M is a little higher than that for LS1.1M and LSM from the TGA evaluation (Figure S3).

In Figure 3b,d, two Mn 2p doublets, i.e., Mn $2p_{1/2}$ and Mn $2p_{3/2}$, can each be deconvoluted into 3 subpeaks. In Mn $2p_{3/2}$, the Mn^{3+} peak is located at ∼640.5 eV, with the Mn^{4+} peak and the Mn satellite (Mn sat') peak at ∼642.5 and ∼643.6 eV, respectively. A-site excessive ions require a decrease of the Mn oxidation state to preserve charge neutrality in LS1.05M. The lattice shrinkage despite the weakened and stretched Mn–O bond or the increased content of trivalent Mn cations in LS1.05M suggests that the Mn–O bond length is not the dominating factor. The influence of the Mn^{3+}/Mn^{4+} redox for ORR and OER will be discussed in later sections. Contents of each oxygen and manganese species are summarized in Table 2.

To investigate the electrochemical performance of perovskite samples, ORR and OER were tested by a three-electrode setup at room temperature in 0.1 M KOH solution. By tuning composition and electronic structure of ORR-oriented LSM, it is expected that its activity of ORR is preserved and that of OER can be enhanced. In Figure 4a, LSM prepared by the PACS method displays ∼45% higher ORR current density at −0.6 V than that from the EDTA-citric acid gel method.[11] The enhancement resulted from the relatively small particle size (fast oxygen diffusion) and synergistic effect between carbon and oxide catalyst (enhanced charge transfer). Furthermore,

DOI: 10.1021/acscatal.9b00800
ACS Catal. 2019, 9, 5074–5083

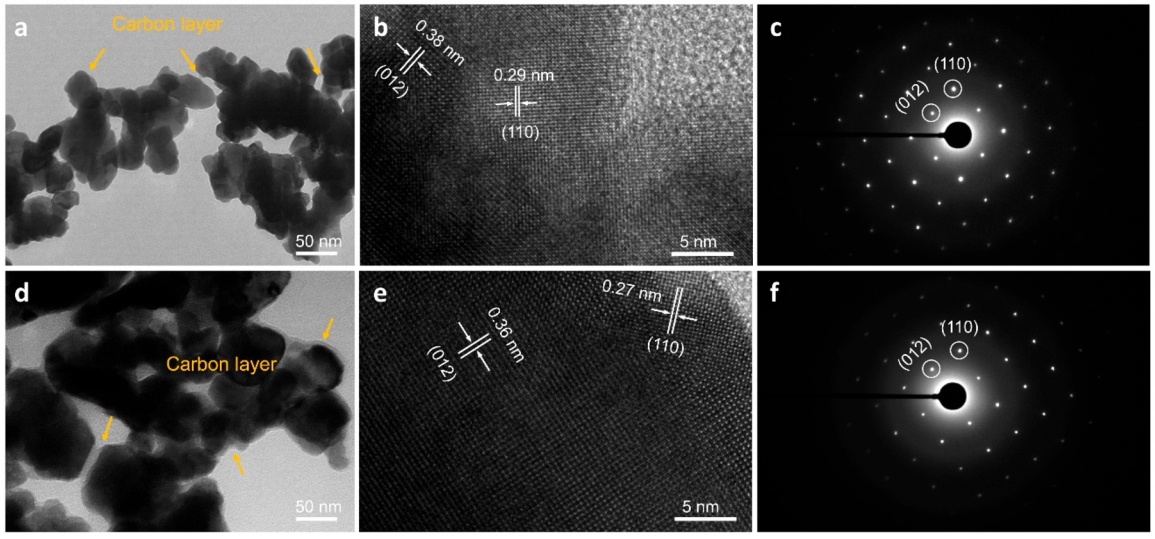

Figure 2. TEM, HRTEM, and SAED for LSM (a–c) and LS1.05M (d–f).

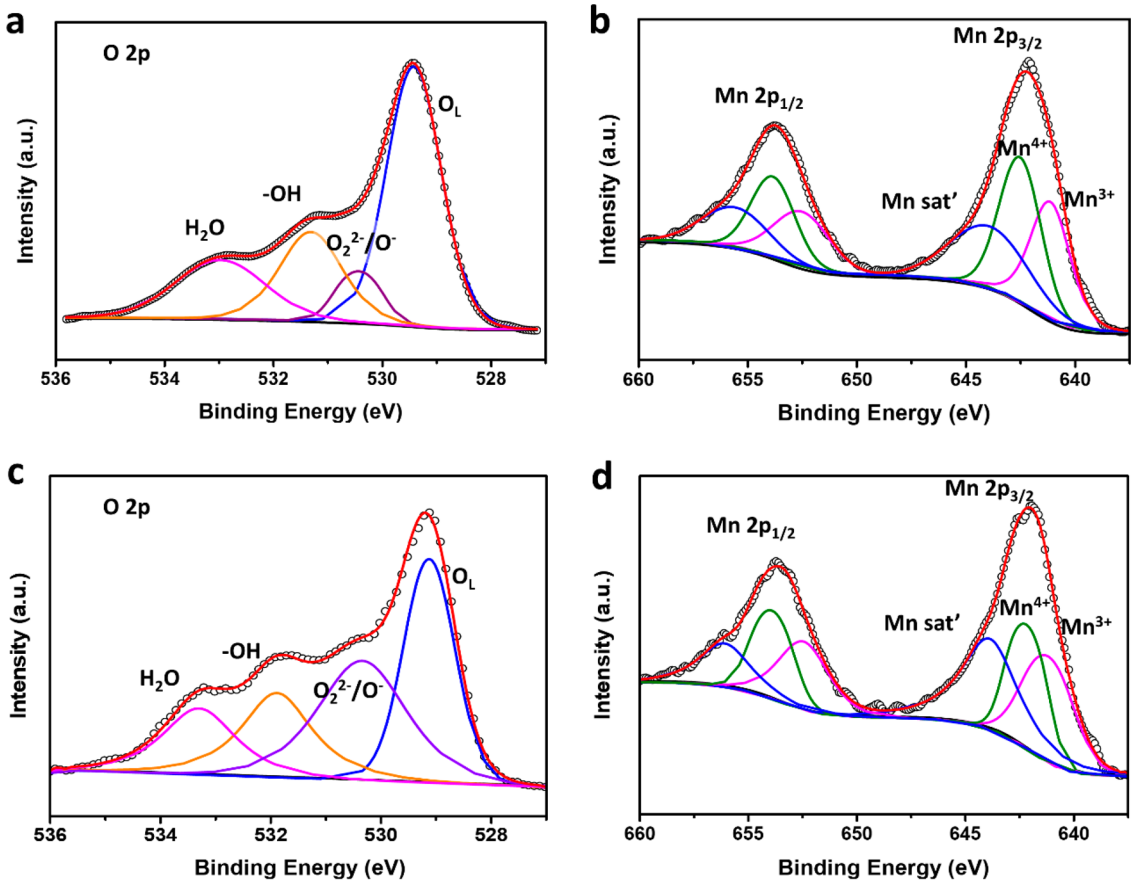

Figure 3. O 2p and Mn 2p XPS for LSM (a, b) and LS1.05M (c, d).

Table 2. XPS of Oxygen and Manganese Contents for LSM and LS1.05M

	O_L	O_2^{2-}/O^-	−OH	H_2O	Mn^{3+}	Mn^{4+}	Mn sat'
LSM	51.7	8.3	20.8	19.2	30.9	38.5	30.6
LS1.05M	32.9	32.1	19.7	15.3	32.8	29.6	37.6

LS1.05M shows 21% higher oxygen-diffusion controlled current density and ca. 10 mV increased half-wave potential compared to our LSM. The O_2^{2-}/O^- species occupied at oxygen vacancy in LS1.05M is responsible for enhanced O_2 molecule adsorption and charge transfer in alkaline solution.[17,49] The polarization curve of LS1.1M gives a 12% ORR current density increase, but the half-wave potential is 100 mV lower relative to LSM. To be noted, catalyst LS1.05M still has an ∼120 mV potential difference at −2 mA cm^{-2} compared to Pt/C.[27] Figure 4b depicts the first-order Koutecky–Levich (K-L) plot confirming mass diffusion-controlled reaction kinetics

DOI: 10.1021/acscatal.9b00800
ACS Catal. 2019, 9, 5074–5083

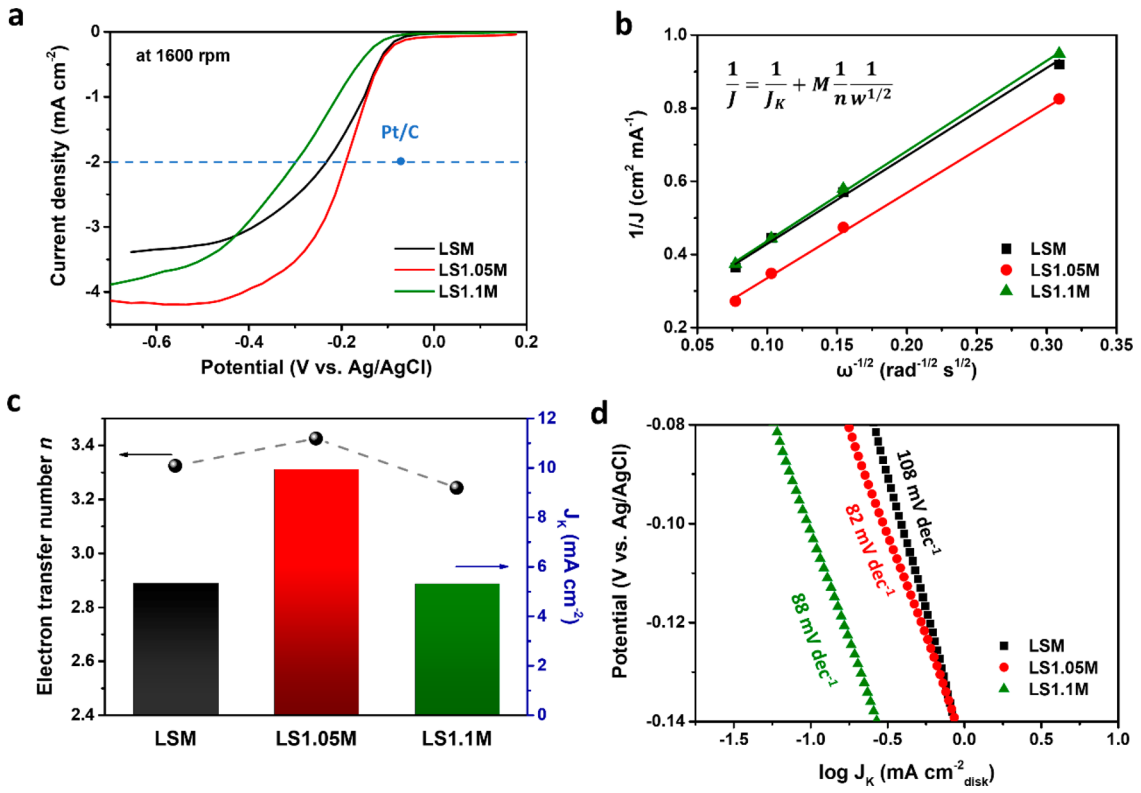

Figure 4. (a) ORR at 1600 rpm and a 20 mV/s scan rate in 0.1 M KOH, (b) Koutecky–Levich plot, (c) electron transfer number and kinetic current density plot, and (d) Tafel plot for LSM, LS1.05M, and LS1.1M.

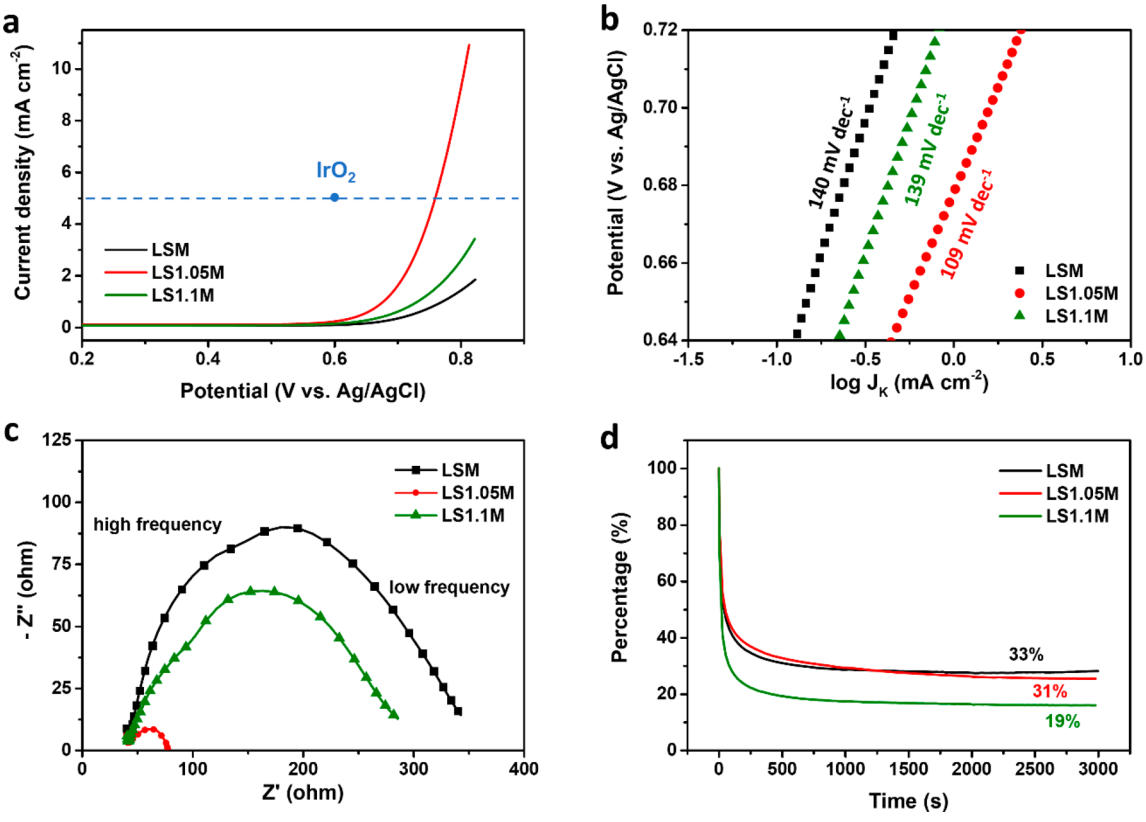

Figure 5. (a) OER of LSM, LS1.05M, and LS1.1M at 900 rpm in 0.1 M KOH solution with a scan rate of 20 mV/s, (b) Tafel plot from 0.62 to 0.72 V, (c) electrochemical impedance spectroscopy from 1 to 100 000 Hz under 5 mV voltage amplitude, and (d) chronoamperometry test at 0.8 V and 1600 rpm for 3000 s.

DOI: 10.1021/acscatal.9b00800
ACS Catal. 2019, 9, 5074−5083

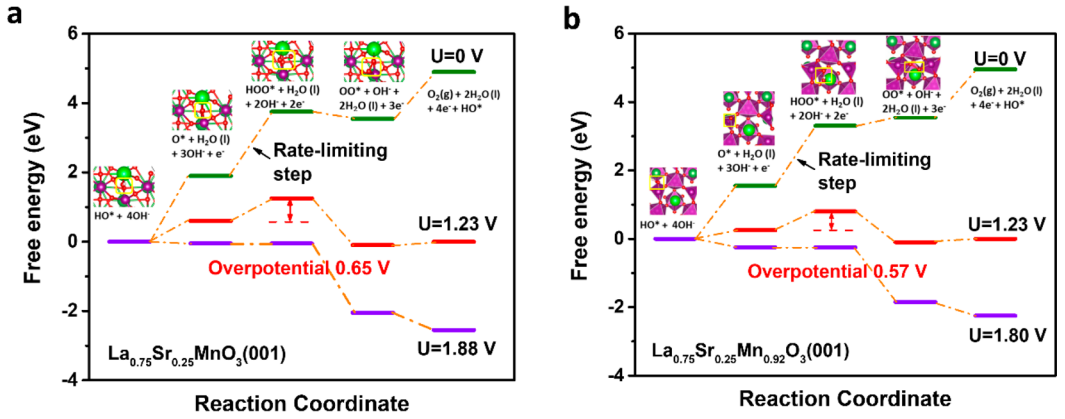

Figure 6. Free energy diagram of a four-step OER mechanism on the (a) $La_{0.75}Sr_{0.25}MnO_3$ and (b) $La_{0.75}Sr_{0.25}Mn_{0.92}O_3$ (001) surface in alkali medium. In all schematics, each purple ball is Mn, fluorescent green ball is Sr, green ball is La, red ball is O, and white ball is H.

at low voltages. In Figure 4c, electron transfer number n and kinetic current density J_K were calculated from the linear fitting results in the K-L plot. ORR of all LSM-based catalysts favor a 4-electron transfer route ($O_2 + 2H_2O + 4e^- \rightarrow 4OH^-$), with LS1.05M reaching 3.4 as the highest ORR efficacy. A massively increased kinetic current density J_K in LS1.05M (~87%) indicates a highly active intrinsic catalyst ORR performance without a substantial change of the reaction mechanism. In Figure 4d, both A-site excessive LSM samples have smaller Tafel slopes compared to LSM. The slopes of LSM, LS1.05M, and LS1.1M are 108, 82, and 88 mV dec^{-1}, respectively. The decreased slope values indicate less demanding voltage at the ORR rate-limiting step.

To investigate OER activity along with electrical impedance and sample stability, linear sweep voltammetry (LSV), electrochemical impedance spectroscopy (EIS), and chronoamperometry (CA) were tested for perovskite samples. In Figure 5a, the maximum OER voltage was set below 1.0 V vs Ag/AgCl (3.5 M) to prevent material dissolving in the electrolyte due to oxygen bubbling on the electrode. Both LS1.05M and LS1.1M show lower overpotential compared to LSM, and the OER current densities show an 8-fold and 1-fold increase at 0.8 V, respectively. The dramatic OER performance improvement results from A-site nonstoichiometry induced oxygen vacancy. The slightly positively charged oxygen vacancy on the catalyst surface attracts OH^- ions in alkaline solution, which benefits oxygen species adsorption on the B-site metal. Compared to IrO_2 performance,[50] a potential gap of ~150 mV for LS1.05M is observed. In Figure 5b, LS1.05M has a Tafel slope of 109 mV dec^{-1}, while the slopes of LSM and LS1.1M are 140 and 139 mV dec^{-1}, respectively. A steep Tafel slope indicates a sluggish current density response to the voltage changes, throttled by the OER rate-limiting step. In Figure 5c, EIS was conducted under a 5 mV amplitude with 1600 rpm rotating speed to reduce oxygen bubble accumulation on the electrode. A-site excessive LS1.05M and LS1.1M samples have a smaller single arc, demonstrating reduced polarization resistance. The ultralow resistivity for LS1.05M was also reported in other 5% A-site excessive or B-site deficient perovskite materials that can be explained by increased oxygen ion mobility and enhanced charge transfer due to a weakened Mn−O bond.[22] In Figure 5d, OER durability at 0.8 V for 3000 s was recorded. Current loss in the first 500 s was observed, with LS1.1M, LS1.05M, and LSM reaching 19%, 31%, and 33% of the initial values, respectively. The stability difference for LSM and LS1.05M was not substantial, but the durability decreases as x in $(La_{0.8}Sr_{0.2})_{1+x}MnO_3$ continues to increase. Transition metals have a strong affinity to oxygen species in solution, and these cations tend to migrate to the catalyst surface,[51] which causes a loss of Mn−O bonds in the lattice especially for LS1.1M with weakened Mn−O bonds and jeopardizes the stability of the material. DFT will be used to understand the mechanism of the effect of A- and B-sites stoichiometry in perovskites on OER activity at the atomic and electronic level as well as the catalyst stability in the following session.

Nominal A-site excessive perovskite is considered as the B-site deficient, as evidenced in XRD and HRTEM. To further understand the defects, the B-site defect formation energy was computed. La to Sr ratio is slightly adjusted for faster converging. Since the B-site (that is, the site occupied by Mn) is the catalytically active center, we examined the Mn-terminated (001) surfaces. The neutral Mn (B-site) defect formation energy was calculated for the $La_{0.75}Sr_{0.25}MnO_3$ (001) surface using the following general formula.[52−56]

$$E_f^v(k, q) = E_{(La_{0.75}Sr_{0.25})_{1.08}Mn_{0.92}O_3,q} - E_{(La_{0.75}Sr_{0.25})MnO_3,q} + N_k\mu_k + q(E_V + \Delta E_f) \quad (6)$$

where $E_f^v(k,q)$ is the defect formation energy for a defect k in the system with charge q. $E_{(La_{0.75}Sr_{0.25})_{1.08}Mn_{0.92}O_3,q}$ is the total energy of the defective system with charge q. $E_{(La_{0.75}Sr_{0.25})MnO_3,q}$ is the total energy of the nondefective system with charge q; N_k is the number of removed species k from the nondefective system, and μ_k is the chemical potential of species k. Note that the chemical potential of species k was chosen by avoiding the precipitation of the elemental metals (La, Mn, and Sr) as well as their metal oxides (La_2O_3, SrO, and Mn_2O_3). q is zero and k is the Mn atom for our neutral B-site defect formation energy calculations. The neutral Mn (B-site) defect formation energy was calculated to be about 0.24 eV under O_2 rich conditions and 2.74 eV under reducing conditions. This defect formation energy value clearly suggests that Mn (B-site) vacancy creation would be much easier in the case of the $La_{0.75}Sr_{0.25}MnO_3$ (001) surface than defect creation in the case of pure $LaMnO_3$.[52] It is also to be noted that, under oxidation conditions, the defect formation energy is thermodynamically more favorable than the reducing conditions.

DOI: 10.1021/acscatal.9b00800
ACS Catal. 2019, 9, 5074−5083

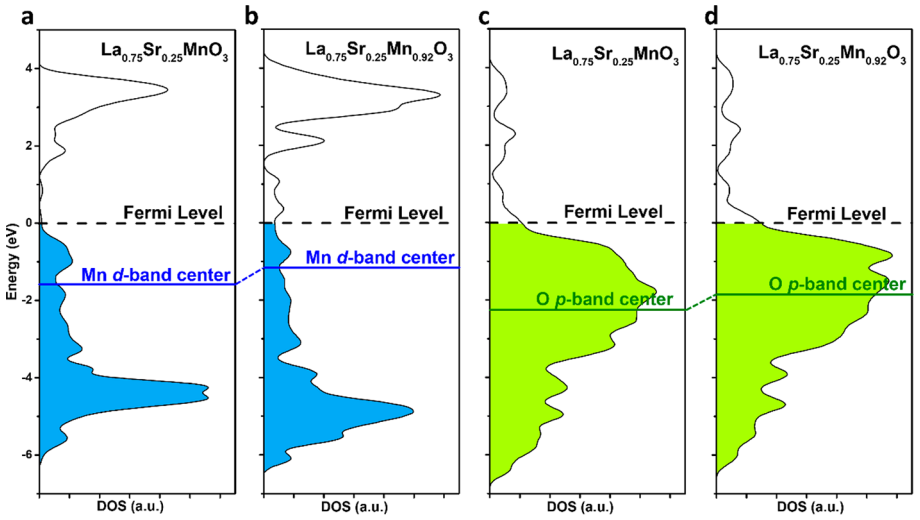

Figure 7. Partial density of states (PDOS) diagrams of surface Mn d-band and Mn d-band center relative to the Fermi surface of $La_{0.75}Sr_{0.25}MnO_3$ (a) and $La_{0.75}Sr_{0.25}Mn_{0.92}O_3$ (b); O p-band and O p-band centers relative to the Fermi surface of $La_{0.75}Sr_{0.25}MnO_3$ (c) and $La_{0.75}Sr_{0.25}Mn_{0.92}O_3$ (d). Note that 0 eV on the *y*-axis is referred to the Fermi energy.

To understand the atomic and electronic level mechanism of the effect of A- and B-sites stoichiometry in perovskites on OER activity, we further resorted to ab initio density functional theory calculations of $La_{0.75}Sr_{0.25}MnO_3$ and $La_{0.75}Sr_{0.25}Mn_{0.92}O_3$ surfaces for the OERs. The results are shown in Figure 6. OERs involved are 4-electron reactions based on the previously reported mechanism in an alkaline medium, where the OER started on the catalyst adsorbed with *OH. The Gibbs free energy of reactions in the whole system at 300 K and 1 atm pressure was estimated from DFT calculations, via thermodynamic and electric-potential energy corrections with reference to the computational hydrogen electrode (CHE) model.[42] Note that the oxygen equilibrium potential is 1.23 V vs CHE. Four different adsorbates *O, *OOH, *OO, and *OH on Mn were evaluated as shown below.

Both free energy patterns share very similar energy profiles, where all the steps are uphill/endothermic, indicating that external electrical potential is necessary to drive the OER. The free energy steps indicate that the largest free energy differences (1.88 and 1.80 eV, respectively, for $La_{0.75}Sr_{0.25}MnO_3$ and $La_{0.75}Sr_{0.25}Mn_{0.92}O_3$) are found for the second step, where O* is converted to *OOH. Hence, the most difficult step in the OERs is the addition of an OH group to adsorbed O* to form adsorbed *OOH. The main reason is that *OOH is weakly bound to the surface as compared to O* bonded to the surface in alkali medium. This could be due to the fact that O* is double bonded to the surface, whereas HOO* is bound with a single bond. The minimum potential at which all reaction steps become downhill in free energy is the measure of the electrocatalytic activity. Free energy diagrams indicate that overpotentials of 0.65 V (1.88−1.23 V) and 0.57 V (1.80−1.23 V) are necessary for $La_{0.75}Sr_{0.25}MnO_3$ and $La_{0.75}Sr_{0.25}Mn_{0.92}O_3$, respectively, to make all steps downhill as exothermal reactions. This result indicates different stoichiometry ratios of A- and B-sites can influence OER kinetics without changing the reaction mechanism. The low overpotential, indicating better OER kinetics, can be explained in the partial density of states (PDOS) diagram of the transition metal d-band center of the surface Mn atom and oxygen 2p band center positions in Figure 7. The PDOS band center was calculated using the equation:[44]

$$\text{band center} = \frac{\int Ef(E)\,dE}{\int f(E)\,dE} \tag{7}$$

where $f(E)$ is the DOS value and E is the electron energy. The results show that the d-band centers are at −1.60 and −1.14 eV, respectively, for $La_{0.75}Sr_{0.25}MnO_3$ and $La_{0.75}Sr_{0.25}Mn_{0.92}O_3$. As the transition metal d-band center shifts toward the Fermi level, one can observe a fraction increase of unoccupied antibonding states formed above the Fermi level,[44] which agrees with increased e_g-filling states (less Mn^{4+}) and enhanced electrocatalytic activity of nominal A-site excessive perovskite in OER performance.

We also calculated PDOS of O p-band and O p-band centers of both $La_{0.75}Sr_{0.25}MnO_3$ and $La_{0.75}Sr_{0.25}Mn_{0.92}O_3$ systems (shown in Figure 7c,d) to check the stability of these systems in alkaline medium. The results indicate that the O p-band centers lie at −2.28 and −1.96 eV, respectively, for $La_{0.75}Sr_{0.25}MnO_3$ and $La_{0.75}Sr_{0.25}Mn_{0.92}O_3$. A strong correlation between oxygen surface exchange kinetics and the position of the bulk O p-band center relative to the Fermi level has been suggested.[57] Also, the computed O p-band center correlates with experimental OER activities of some perovskites in alkaline solution.[52] Our PDOS diagrams agree with perovskite electrochemical tests. Though oxygen p-band center positions are neither too close nor too far away from the Fermi level,[43,58] as they approach the Fermi level, a decrease of oxygen vacancy formation energy can potentially destabilize the perovskite phase.[44] As the nominal A-site excess amount increases, reduced stability of perovskite can be explained with the O p-band center passing a threshold value of −2.20 V, resulting in reduced oxygen bonding strength, higher oxygen vacancy concentration, and lattice oxygen mobility.[43]

4. CONCLUSIONS

Nominal A-site excessive LS1.05M and LS1.1M were prepared by the PACS method, and the electrochemical performance was tested and compared with LSM. With a 5% excess of A-site cations, LS1.05M shows a contracted lattice, larger surface

DOI: 10.1021/acscatal.9b00800
ACS Catal. 2019, 9, 5074−5083

area, and higher content of active oxygen species. The electrochemical performance was enhanced especially in OER. LS1.1M also shows superior performance to LSM but is not comparable to LS1.05M, probably due to lattice instability from excessive A-site nonstoichiometry and oxygen defects. Performance improvement of A-site excessive LS1.05M and LS1.1M is attributed to transition metal d-band center upshift and oxygen p-band center approaching the Fermi level. The increased fraction of antibonding states and oxygen vacancy concentration reduce the OER free energy of O* converting to *OOH at the rate-limiting step. The overall enhanced ORR and OER catalytic abilities suggest that A-site excess (or B-site deficiency) is a simple and effective strategy for perovskite catalyst modification.

■ ASSOCIATED CONTENT

Supporting Information

The Supporting Information is available free of charge on the ACS Publications website at DOI: 10.1021/acscatal.9b00800.

ICP-ORS, SEM-EDX mapping, and EDX spectra; X-ray fluorescence (XRF) results for LSM, LS1.05M, and LS1.1M; XRD refinement results from Maud; surface elemental ratio for LSM, LS1.05M, and LS1.1M by XPS; TGA and BET results for LSM, LS1.05M, and LS1.1M (PDF)

■ AUTHOR INFORMATION

Corresponding Authors

*E-mail: mzhou@nmsu.edu (M.Z.).
*E-mail: hluo@nmsu.edu (H.L.).
*E-mail: pabitra.choudhury@nmt.edu (P.C.).
*E-mail: dong.ding@inl.gov (D.D.).

ORCID

Gen Chen: 0000-0003-3504-3572
Dong Ding: 0000-0002-6921-4504
Pabitra Choudhury: 0000-0002-5023-9154
Hongmei Luo: 0000-0002-9546-761X

Notes

The authors declare no competing financial interest.

■ ACKNOWLEDGMENTS

This work was supported by New Mexico EPSCoR with NSF-1301346 and the Idaho National Laboratory Directed Research and Development Program under DOE Idaho Operations Office Contract DE-AC07-05ID14517. DFT work is supported by ACS-PRF [58740-UR6] and used the Extreme Science and Engineering Discovery Environment (XSEDE) TACC at the stampede2 through allocation [TG-DMR140131].

■ REFERENCES

(1) Zhu, Y.; Zhou, W.; Yu, J.; Chen, Y.; Liu, M.; Shao, Z. Enhancing Electrocatalytic Activity of Perovskite Oxides by Tuning Cation Deficiency for Oxygen Reduction and Evolution Reactions. *Chem. Mater.* **2016**, *28*, 1691−1697.

(2) Reier, T.; Oezaslan, M.; Strasser, P. Electrocatalytic Oxygen Evolution Reaction (Oer) on Ru, Ir, and Pt Catalysts: A Comparative Study of Nanoparticles and Bulk Materials. *ACS Catal.* **2012**, *2*, 1765−1772.

(3) Escalante-García, I.; Duron-Torres, S.; Cruz, J.; Arriaga-Hurtado, L. Electrochemical Characterization of IrO_2-Pt and RuO_2-Pt Mixtures as Bifunctional Electrodes for Unitized Regenerative Fuel Cells. *J. New Mater. Electrochem. Syst.* **2010**, *13*, 161−299.

(4) Bursell, M.; Pirjamali, M.; Kiros, Y. $La_{0.6}Ca_{0.4}CoO_3$, $La_{0.1}Ca_{0.9}MnO_3$ and $LaNiO_3$ as Bifunctional Oxygen Electrodes. *Electrochim. Acta* **2002**, *47*, 1651−1660.

(5) Yan, L.; Ding, H.; Zhu, Z.; Xue, X. Investigation of Cobalt-Free Perovskite $Ba_{0.95}$ $La_{0.05}FeO_3$ as a Cathode for Proton-Conducting Solid Oxide Fuel Cells. *J. Power Sources* **2011**, *196*, 9352−9355.

(6) Zhang, P.; Guan, G.; Khaerudini, D. S.; Hao, X.; Han, M.; Kasai, Y.; Sasagawa, K.; Abudula, A. Properties of a-Site Nonstoichiometry $(Pr_{0.4})_XSr_{0.6}Co_{0.2}Fe_{0.7}Nb_{0.1}O_3$ ($0.9 \leq X \leq 1.1$) as Symmetrical Electrode Material for Solid Oxide Fuel Cells. *J. Power Sources* **2014**, *248*, 163−171.

(7) Zuo, R.; Su, S.; Wu, Y.; Fu, J.; Wang, M.; Li, L. Influence of a-Site Nonstoichiometry on Sintering, Microstructure and Electrical Properties of $(Bi_{0.5}$ $na_{0.5})Tio_3$ Ceramics. *Mater. Chem. Phys.* **2008**, *110*, 311−315.

(8) Yang, D.; Yang, N.; Meng, B.; Tan, X.; Zhang, C.; Sunarso, J.; Zhu, Z.; Liu, S. A-Site Excess $(La_{0.8}Ca_{0.2})_{1.01}FeO_3$ (LCF) Perovskite Hollow Fiber Membrane for Oxygen Permeation in Co_2-Containing Atmosphere. *Energy Fuels* **2017**, *31*, 4531−4538.

(9) Kharton, V.; Kovalevsky, A.; Tsipis, E.; Viskup, A.; Naumovich, E.; Jurado, J.; Frade, J. Mixed Conductivity and Stability of a-Site-Deficient $Sr(Fe,Ti)O_3$ Perovskites. *J. Solid State Electrochem.* **2002**, *7*, 30−36.

(10) Lu, Z.; Zhang, H.; Lei, W.; Sinclair, D. C.; Reaney, I. M. High-Figure-of-Merit Thermoelectric La-Doped a-Site-Deficient $Srtio_3$ Ceramics. *Chem. Mater.* **2016**, *28*, 925−935.

(11) Jin, C.; Cao, X.; Zhang, L.; Zhang, C.; Yang, R. Preparation and Electrochemical Properties of Urchin-Like $La_{0.8}Sr_{0.2}MnO_3$ Perovskite Oxide as a Bifunctional Catalyst for Oxygen Reduction and Oxygen Evolution Reaction. *J. Power Sources* **2013**, *241*, 225−230.

(12) Lu, F.; Sui, J.; Su, J.; Jin, C.; Shen, M.; Yang, R. Hollow Spherical $La_{0.8}Sr_{0.2}MnO_3$ Perovskite Oxide with Enhanced Catalytic Activities for the Oxygen Reduction Reaction. *J. Power Sources* **2014**, *271*, 55−59.

(13) Vu, N. N.; Nguyen, C. C.; Kaliaguine, S.; Do, T. O. Reduced Cu/Pt−$HCa_2Ta_3O_{10}$Perovskite Nanosheets for Sunlight-Driven Conversion of CO_2 into Valuable Fuels. *Adv. Sustainable Syst.* **2017**, *1*, 1700048.

(14) Gao, Y.; Wang, J.; Lyu, Y.-Q.; Lam, K.; Ciucci, F. In Situ Growth of Pt_3Ni Nanoparticles on an a-Site Deficient Perovskite with Enhanced Activity for the Oxygen Reduction Reaction. *J. Mater. Chem. A* **2017**, *5*, 6399−6404.

(15) Zhang, H.; Shimizu, Y.; Teraoka, Y.; Miura, N.; Yamazoe, N. Oxygen Sorption and Catalytic Properties of $La_{1-X}Sr_xCo_{1-Y}Fe_yO_3$Perovskite-Type Oxides. *J. Catal.* **1990**, *121*, 432−440.

(16) Merino, N. A.; Barbero, B. P.; Eloy, P.; Cadús, L. E. $La_{1-X}Ca_XCoO_3$ Perovskite-Type Oxides: Identification of the Surface Oxygen Species by Xps. *Appl. Surf. Sci.* **2006**, *253*, 1489−1493.

(17) Wang, Z.; You, Y.; Yuan, J.; Yin, Y.-X.; Li, Y.-T.; Xin, S.; Zhang, D. Nickel-Doped $La_{0.8}Sr_{0.2}Mn_{1-X}Ni_XO_3$ Nanoparticles Containing Abundant Oxygen Vacancies as an Optimized Bifunctional Catalyst for Oxygen Cathode in Rechargeable Lithium−Air Batteries. *ACS Appl. Mater. Interfaces* **2016**, *8*, 6520−6528.

(18) Yan, L.; Lin, Y.; Yu, X.; Xu, W.; Salas, T.; Smallidge, H.; Zhou, M.; Luo, H. $La_{0.8}Sr_{0.2}MnO_3$−Based Perovskite Nanoparticles with the a-Site Deciency as High Performance Bifunctional Oxygen Catalyst in Alkaline Solution. *ACS Appl. Mater. Interfaces* **2017**, *9*, 23820−23827.

(19) Yang, Y.; Chen, Y.; Tian, D.; Lu, X.; Ding, Y.; Yu, W.; Lin, B. A New a-Site Excessive Strategy to Improve Performance of Layered Perovskite Cathode for Intermediate-Temperature Solid Oxide Fuel Cells. *Electrochim. Acta* **2017**, *231*, 686−693.

(20) Zhou, W.; Ran, R.; Shao, Z.; Zhuang, W.; Jia, J.; Gu, H.; Jin, W.; Xu, N. Barium- and Strontium-Enriched $(Ba_{0.5}Sr_{0.5})_{1+x}Co_{0.8}Fe_{0.2}O_{3-delta}$ Oxides as High-Performance Cathodes for Intemediate-Temperature Solid-Oxide Fuel Cells. *Acta Mater.* **2008**, *56*, 2687−2698.

DOI: 10.1021/acscatal.9b00800
ACS Catal. 2019, 9, 5074−5083

(21) Chen, J.; Shen, M.; Wang, X.; Qi, G.; Wang, J.; Li, W. The Influence of Nonstoichiometry on $LaMnO_3$ Perovskite for Catalytic No Oxidation. *Appl. Catal., B* **2013**, *134*, 251−257.
(22) Li, M.; Zhang, H.; Cook, S. N.; Li, L.; Kilner, J. A.; Reaney, I. M.; Sinclair, D. C. Dramatic Influence of a-Site Nonstoichiometry on the Electrical Conductivity and Conduction Mechanisms in the Perovskite Oxide $Na_{0.5}Bi_{0.5}TiO_3$. *Chem. Mater.* **2015**, *27*, 629−634.
(23) Li, M.; Pietrowski, M. J.; De Souza, R. A.; Zhang, H.; Reaney, I. M.; Cook, S. N.; Kilner, J. A.; Sinclair, D. C. A Family of Oxide Ion Conductors Based on the Ferroelectric Perovskite $Na_{0.5}Bi_{0.5}TiO_3$. *Nat. Mater.* **2014**, *13*, 31.
(24) Deng, F.; Zhou, X.; Ma, J.; Jiang, C.; Meng, G.; Liu, X. Characterization of a-Site Excessive Perovskite $La_{0.7-X}Sm_{X+0.02}Ca_{0.3}CrO_3$. *J. Rare Earths* **2009**, *27*, 227−230.
(25) Cai, G.; Cheng, X.; Layani, M.; Tan, A. W. M.; Li, S.; Eh, L. S.; Gao, D.; Magdassi, S.; Lee, P. S. Direct inkjet-patterning of energy efficient flexible electrochromics. *Nano Energy* **2018**, *49*, 147.
(26) Hua, B.; Sun, Y.; Li, M.; Yan, N.; Chen, J.; Zhang, Y.; Zeng, Y. M.; Amirkhiz, B.; Luo, J. L. Stabilizing Double Perovskite for Effective Bifunctional Oxygen Electrocatalysis in Alkaline Conditions. *Chem. Mater.* **2017**, *29*, 6228.
(27) Xu, W.; Yan, L.; Teich, L.; Liaw, S.; Zhou, M.; Luo, H. Polymer-Assisted Chemical Solution Synthesis of $La_{0.8}Sr_{0.2}MnO_3$Based Perovskite with a-Site Deficiency and Cobalt-Doping for Bifunctional Oxygen Catalyst in Alkaline Media. *Electrochim. Acta* **2018**, *273*, 80−87.
(28) Jia, Q.; McCleskey, T. M.; Burrell, A.; Lin, Y.; Collis, G.; Wang, H.; Li, A.; Foltyn, S. Polymer-Assisted Deposition of Metal-Oxide Films. *Nat. Mater.* **2004**, *3*, 529.
(29) Perdew, J. P.; Burke, K.; Ernzerhof, M. Generalized Gradient Approximation Made Simple. *Phys. Rev. Lett.* **1996**, *77*, 3865−3868.
(30) Kresse, G.; Joubert, D. From Ultrasoft Pseudopotentials to the Projector Augmented-Wave Method. *Phys. Rev. B: Condens. Matter Mater. Phys.* **1999**, *59*, 1758−1775.
(31) Kresse, G.; Furthmüller, J. Efficiency of Ab-Initio Total Energy Calculations for Metals and Semiconductors Using a Plane-Wave Basis Set. *Comput. Mater. Sci.* **1996**, *6*, 15−50.
(32) Kresse, G.; Furthmüller, J. Efficient Iterative Schemes for \Textit{Ab Initio} Total-Energy Calculations Using a Plane-Wave Basis Set. *Phys. Rev. B: Condens. Matter Mater. Phys.* **1996**, *54*, 11169−11186.
(33) Kresse, G.; Hafner, J. Ab Initio Molecular Dynamics for Liquid Metals. *Phys. Rev. B: Condens. Matter Mater. Phys.* **1993**, *47*, 558−561.
(34) Grimme, S. Semiempirical Gga-Type Density Functional Constructed with a Long-Range Dispersion Correction. *J. Comput. Chem.* **2006**, *27*, 1787−1799.
(35) Wang, L.; Maxisch, T.; Ceder, G. Oxidation Energies of Transition Metal Oxides within the Gga+U Framework. *Phys. Rev. B: Condens. Matter Mater. Phys.* **2006**, *73*, 195107.
(36) Curnan, M. T.; Kitchin, J. R. Effects of Concentration, Crystal Structure, Magnetism, and Electronic Structure Method on First-Principles Oxygen Vacancy Formation Energy Trends in Perovskites. *J. Phys. Chem. C* **2014**, *118*, 28776−28790.
(37) Mussell, S.; Choudhury, P. Density Functional Theory Study of Iron Phthalocyanine Porous Layer Deposited on Graphene Substrate: A Pt-Free Electrocatalyst for Hydrogen Fuel Cells. *J. Phys. Chem. C* **2016**, *120*, 5384−5391.
(38) Ghysels, A.; Verstraelen, T.; Hemelsoet, K.; Waroquier, M.; Van Speybroeck, V. Tamkin: A Versatile Package for Vibrational Analysis and Chemical Kinetics. *J. Chem. Inf. Model.* **2010**, *50*, 1736−1750.
(39) Ghysels, A.; Van Speybroeck, V.; Verstraelen, T.; Van Neck, D.; Waroquier, M. Calculating Reaction Rates with Partial Hessians: Validation of the Mobile Block Hessian Approach. *J. Chem. Theory Comput.* **2008**, *4*, 614−625.
(40) Choudhury, P.; Bhethanabotla, V. R.; Stefanakos, E. Manganese Borohydride as a Hydrogen-Storage Candidate: First-Principles Crystal Structure and Thermodynamic Properties. *J. Phys. Chem. C* **2009**, *113*, 13416−13424.
(41) Nie, X.; Luo, W.; Janik, M. J.; Asthagiri, A. Reaction Mechanisms of Co_2 Electrochemical Reduction on Cu(111) Determined with Density Functional Theory. *J. Catal.* **2014**, *312*, 108−122.
(42) NØrskov, J. K.; Rossmeisl, J.; Logadottir, A.; Lindqvist, L.; Kitchin, J. R.; Bligaard, T.; Jónsson, H. Origin of the Overpotential for Oxygen Reduction at a Fuel-Cell Cathode. *J. Phys. Chem. B* **2004**, *108*, 17886−17892.
(43) Zhao, B.; Zhang, L.; Zhen, D.; Yoo, S.; Ding, Y.; Chen, D.; Chen, Y.; Zhang, Q.; Doyle, B.; Xiong, X.; Liu, M. A Tailored Double Perovskite Nanofiber Catalyst Enables Ultrafast Oxygen Evolution. *Nat. Commun.* **2017**, *8*, 14586.
(44) Hong, W. T.; Risch, M.; Stoerzinger, K. A.; Grimaud, A.; Suntivich, J.; Shao-Horn, Y. Toward the Rational Design of Non-Precious Transition Metal Oxides for Oxygen Electrocatalysis. *Energy Environ. Sci.* **2015**, *8*, 1404−1427.
(45) Zhou, W.; Ran, R.; Shao, Z.; Jin, W.; Xu, N. Evaluation of A-Site Cation-Deficient $(Ba_{0.5}Sr_{0.5})_{1-chi}Co_{0.8}Fe_{0.2}O_3$(chi (0) Perovskite as a Solid-Oxide Fuel Cell Cathod. *J. Power Sources* **2008**, *182*, 24−31.
(46) Tsvetkov, N.; Lu, Q.; Sun, L.; Crumlin, E. J.; Yildiz, B. Improved Chemical and Electrochemical Stability of Perovskite Oxides with Less Reducible Cations at the Surface. *Nat. Mater.* **2016**, *15*, 1010−6.
(47) Mueller, D. N.; Machala, M. L.; Bluhm, H.; Chueh, W. C. Redox Activity of Surface Oxygen Anions in Oxygen-Deficient Perovskite Oxides During Electrochemical Reactions. *Nat. Commun.* **2015**, *6*, 6097.
(48) Mefford, J. T.; Rong, X.; Abakumov, A. M.; Hardin, W. G.; Dai, S.; Kolpak, A. M.; Johnston, K. P.; Stevenson, K. J. Water Electrolysis on $La_{1-x}Sr_xCoO_3$Perovskite Electrocatalyst. *Nat. Commun.* **2016**, *7*, 11053.
(49) Du, J.; Zhang, T.; Cheng, F.; Chu, W.; Wu, Z.; Chen, J. Nonstoichiometric Perovskite $CaMnO_3$ for Oxygen Electrocatalysis with High Activity. *Inorg. Chem.* **2014**, *53*, 9106−9114.
(50) Zhao, Y.; Kamiya, K.; Hashimoto, K.; Nakanishi, S. Efficient Bifunctional Fe/C/N Electrocatalysts for Oxygen Reduction and Evolution Reaction. *J. Phys. Chem. C* **2015**, *119*, 2583−2588.
(51) Balbuena, P.; Callejas-Tovar, R.; Hirunsit, P. d.; De La Hoz, J. M.; Ma, Y.; Ramirez-Caballero, G. Evolution of Pt and Pt-Alloy Catalytic Surfaces under Oxygen Reduction Reaction in Acid Medium. *Top. Catal.* **2012**, *55*, 322−335.
(52) Olsson, E.; Aparicio-Anglès, X.; de Leeuw, N. H. Ab Initio Study of Vacancy Formation in Cubic $LaMnO_3$ and $SmCoO_3$ as Cathode Materials in Solid Oxide Fuel Cells. *J. Chem. Phys.* **2016**, *145*, 014703.
(53) Lee, Y.-L.; Morgan, D. Ab Initio Defect Energetics of Perovskite (001) Surfaces for Solid Oxide Fuel Cells: A Comparative Study of LaMnO3 Versus $SrTiO_3$ and $LaAlO_3$. *Phys. Rev. B: Condens. Matter Mater. Phys.* **2015**, *91*, 195430.
(54) Gu, M.; Wang, Z.; Biegalski, M. D.; Christen, H. M.; Takamura, Y.; Browning, N. D. Antisite Defects in $La_{0.7}Sr_{0.3}MnO_3$ and $La_{0.7}Sr_{0.3}FeO_3$. *Appl. Phys. Lett.* **2013**, *102*, 151911.
(55) Piskunov, S.; Heifets, E.; Jacob, T.; Kotomin, E. A.; Ellis, D. E.; Spohr, E. Electronic Structure and Thermodynamic Stability of $LaMnO_3$ and $La_{1-x}Sr_xMnO_3$ (001) Surfaces: Ab Initio Calculations. *Phys. Rev. B: Condens. Matter Mater. Phys.* **2008**, *78*, 121406R.
(56) Alahmed, Z.; Fu, H. First-Principles Determination of Chemical Potentials and Vacancy Formation Energies in $PbTiO_3$ and $BaTiO_3$. *Phys. Rev. B: Condens. Matter Mater. Phys.* **2007**, *76*, 224101.
(57) Lee, Y.-L.; Kleis, J.; Rossmeisl, J.; Shao-Horn, Y.; Morgan, D. Prediction of Solid Oxide Fuel Cell Cathode Activity with First-Principles Descriptors. *Energy Environ. Sci.* **2011**, *4*, 3966−3970.
(58) Grimaud, A.; May, K. J.; Carlton, C. E.; Lee, Y.-L.; Risch, M.; Hong, W. T.; Zhou, J.; Shao-Horn, Y. Double Perovskites as a Family of Highly Active Catalysts for Oxygen Evolution in Alkaline Solution. *Nat. Commun.* **2013**, *4*, 2439.

DOI: 10.1021/acscatal.9b00800
ACS Catal. 2019, 9, 5074−5083